



Focal-ratio degradation (FRD) mitigation in a multimode fibre link using mode-selective photonic lanterns

Aurélien Benoît¹,¹★ Stephanos Yerolatsitis²,² Kerrianne Harrington,² Tim A. Birks² and Robert R. Thomson¹

¹*SUPA, Institute of Photonics and Quantum Sciences, Heriot-Watt University, Edinburgh EH14 4AS, UK*

²*Department of Physics, University of Bath, Claverton Down, Bath BA2 7AY, UK*

Accepted 2020 December 11. Received 2020 December 11; in original form 2020 June 4

ABSTRACT

We present a new way to mitigate focal-ratio degradation (FRD) when using optical fibres to transport multimode light. Our approach exploits a custom multicore fibre (MCF) with six dissimilar cores that are single-mode at ~ 1550 nm wavelength and minimally coupled over 7 m. We fabricated adiabatic mode-selective photonic lanterns (PLs) at each end of the MCF to create a fibre link with multimode ports, the PLs coupling each spatial mode of the multimode ports to a specific core of the MCF and vice versa. The PL-MCF-PL link exhibits superior FRD behaviour compared to a conventional multimode fibre that also supports six modes, because it inhibits the transfer of light from lower order modes to higher order modes. These results open up a potential powerful new approach to mitigate FRD in multimode fibre links, with particular applications in astronomical instruments.

Key words: instrumentation: miscellaneous – instrumentation: spectrograph – methods: data analysis – techniques: miscellaneous – techniques: spectroscopic.

1 INTRODUCTION

Optical fibres provide a powerful way to route light with low loss, and are one of the most ubiquitous photonic technologies. As such, they have become enabling in areas such as telecommunications (Richardson 2013), laser-based industrial manufacturing (Malinauskas 2012), biomedical instrumentation (Li 2018), and physical / chemical environmental sensors (Yin 2018). One area that has also been transformed by low-loss fibre is optical- and near-infrared astronomical instrumentation, where fibres can be used to efficiently and flexibly route light from the telescope focal plane to a spectrograph for wavelength-resolved analysis (Angel 1977). In such applications, fibres facilitate the complete mechanical de-coupling of the spectrograph from the telescope. As a result, the spectrograph can be placed in an environmentally stabilized room in the observatory, maximizing optomechanical stability (Barden 1994). The fibre link is therefore a key component in instruments such as HARPS that are capable of measuring spectral shifts in stellar spectra on the order of 1 part in 10^{10} between 380 and 690 nm, which corresponds to detecting a radial velocity shift due to a planetary companion of ~ 10 cm s⁻¹ (Mayor 2003).

Maximizing the optomechanical stability of instruments is not the only advantage that fibres can provide. In multi-object and diverse-field spectrographs, fibres can route light from many different parts of the telescope focal plane to the spectrograph. The ability of fibres to provide high ‘multiplex gain’ in this manner has been exploited in numerous astronomical instruments. A notable example included 2dF (Colless 2001), where hundreds of multimode fibres (MMFs)

were used to route light from selectable regions across the focal plane to the AAOmega spectrograph for simultaneous analysis. Highly multiplexed observations by 2dF have provided remarkable insights into the large-scale structure of the universe, such as the existence of baryon acoustic oscillations (Colless 2001).

Despite the numerous advantages of fibres, they are not without drawbacks. One example is focal-ratio degradation (FRD; Barden 1981; Ramsey 1988), where light at the output of a fibre emerges with a lower f-number (higher numerical aperture (NA)) than the injected light. For photon-starved astronomical applications, the input f-ratio is generally controlled to maximize telescope-to-fibre coupling efficiency. However, if the f-ratio is then lowered by a fibre with FRD feeding an instrument downstream, the resulting ‘faster’ beam of light requires larger instrument optics to deliver the same efficiency and spectroscopic resolution. This results in more expensive instruments and lower quality optics (Parry 2006). Techniques that efficiently mitigate FRD in fibre-fed spectrographs are therefore of considerable interest, and MMF links that are immune to FRD would have profound implications on the design of future systems.

From the perspective of guided-wave optics, FRD is the result of mode coupling along the fibre due to microbending or core deformations. This mode coupling can transfer light from lower order modes to higher order modes (Clayton 1989; Carrasco & Parry 1994). Since higher order modes emerge from the output of the fibre with a lower f-ratio than lower order modes, mode-coupling induces FRD. For a photonic point of view, the f-ratio is directly linked to the numerical aperture NA with the relation $f/\# = (2\text{NA})^{-1}$. For all the f-ratio evolutions in this paper, we present the linked NA value on a second axis. Fig. 1 illustrates how the f-ratio of light emerging

* E-mail: a.benoit@hw.ac.uk

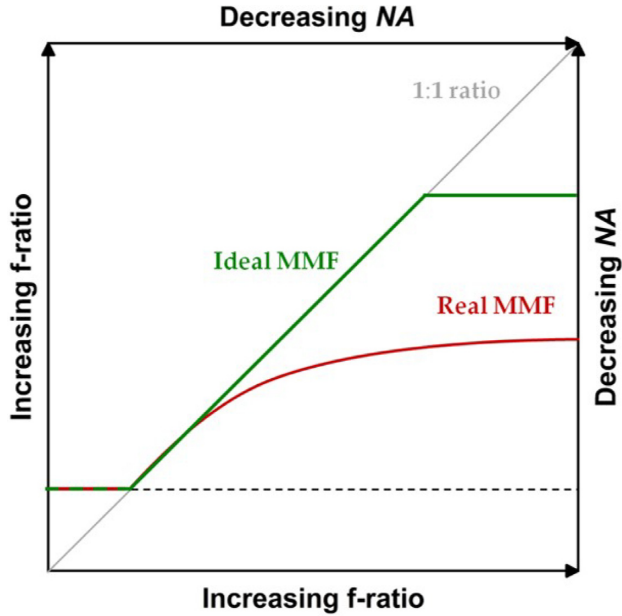


Figure 1. Representation of how FRD would manifest in ideal (green) and real (red) MMF. The solid grey line represents the line along which no FRD would be generated.

from a fibre might vary with input f-ratio, when using either an ideal MMF without FRD (green line) or a real MMF with FRD (red lines). In the ideal case, the output f-ratio matches the input f-ratio between two limits – the upper limit being the f-ratio of the fundamental mode of the fibre, and the lower limit being the f-ratio of the highest order guided mode. In real MMFs, however, the output f-ratio is reduced compared to the input f-ratio, with the difference becoming particularly pronounced as the input f-ratio increases. Any FRD mitigation technology is aimed at achieving a fibre link with FRD properties closer to the ideal characteristic shown in Fig. 1, while still maintaining throughput efficiency.

The FRD behaviour of MMFs has been intensively studied. The work has focused on understanding the impact of the MMF core diameter (Ramsey 1988; Oliveira, de Oliveira & dos Santos 2005; Yan 2018), core geometry (Horton 2011), wavelength (Poppett & Allington-Smith 2007; Murphy 2008), bending stress (Carrasco & Parry 1994), and MMF length (Yan 2017), and has also been extended to the case of bundles of MMFs (Bryant 2012, 2014). In all of these cases, the MMFs follow the trend represented by the red curve in Fig. 1.

Over the last decade, fibre technology called the photonic lantern (PL) has been developed which has the potential to transform the operation of MMF-fed astronomical instruments by efficiently interfacing multimode astronomical signals with single-mode (SM) photonic devices. The basic idea is shown in Fig. 2, where a gradual optical transition connects the spatial modes of an MMF core to a set of discrete single-mode cores (Leon-Saval 2005; Noordegraaf 2009). In general the connection is one-to-many: light contained in one spatial mode of the MMF is distributed between most or all of the single-mode cores, and vice versa. By designing the PL correctly, it conserves the number of guided modes in both directions (Leon-Saval 2005; Birks 2012, 2015). Several astrophotonics applications for PLs have been proposed, including in OH-line suppression (Bland-Hawthorn 2011), mode scramblers (Gris-Sánchez 2018), and for reformatting multimode light for diffraction-limited spectroscopy (Bland-Hawthorn 2010; Birks 2012; MacLachlan 2017).

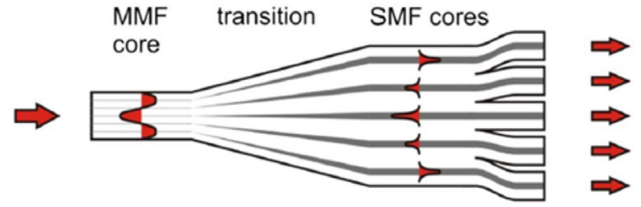


Figure 2. Schematic diagram of a PL made by tapering a bundle of single-mode fibres. From right to left: separate SMFs are fused together to form a single glass body, which simultaneously reduces in cross-sectional scale to form an MMF core. Surrounding it is a low-index jacket (not shown) that forms a cladding for the MMF core (Leon-Saval 2005; Birks 2015).

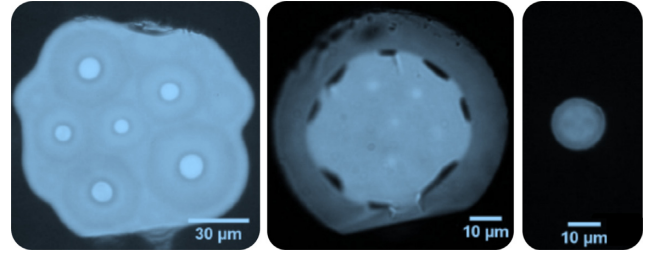


Figure 3. Optical micrographs of (left-hand panel) the MCF, (centre) the MCF with an F-doped silica jacket collapsed on to it part-way along the transition, and (right-hand panel) the multimode port of a mode-selective PL.

Here, we demonstrate the feasibility of this new route to mitigate FRD in multimode fibre links based on mode-selective PLs (Yerolatsitis 2017). In contrast to conventional PLs, in a mode-selective PL the connection between modes and cores is one-to-one: light in one mode of the MMF is routed to one specific single-mode core (a different one for each mode), and vice-versa. Our proposed MMF link is a multicore fibre (MCF) with mode-selective PLs at either end. If the MCF is designed to avoid intercore coupling along its length, the whole PL-MCF-PL link preserves the power distribution across the modes between input and output, preventing FRD. In principle, there is no limit to the number of modes as long as the taper adiabatic criterion is satisfied. Spectral bandwidth is only limited by the need to have at least as many MCF cores as MMF modes at the shortest wavelength. However, it is important to note that for shorter wavelengths the individual cores may no longer be single-mode, which in turn will affect the adiabatic operation of the device.

The paper is structured as follows. We characterize the six-core MCF in Section 2 and the mode-selective PLs made from it in Section 3. In Section 4, we demonstrate the PL-MCF-PL multimode fibre link. In Section 5, we present the conclusions of the paper.

2 THE MULTICORE FIBRE

Our MCF had six Ge-doped step-index cores with dissimilar diameters of 11, 10.3, 9.5, 8.3, 7.3, and 6.5 μm (Fig. 3). Their minimum separation was 26 μm , which simulations indicated would ensure cross-talk remained below 0.08 per cent after 2 m of MCF (Yerolatsitis 2017). To study its guiding properties, we coupled light of wavelength 1550 ± 20 nm from a thermal source into a 1 m length of a single-mode telecoms fibre (SMF-28). We excited each MCF core individually using direct fibre-to-fibre butt excitation, with fibre alignment optimized for maximum transmission. Near-field images of the MCF output taken with a high sensitivity InGaAs Hamamatsu camera with a linear range of 1:16000, Figs 4(a) and (f), demonstrate that there is negligible cross-talk between the cores over 1.5 m. These

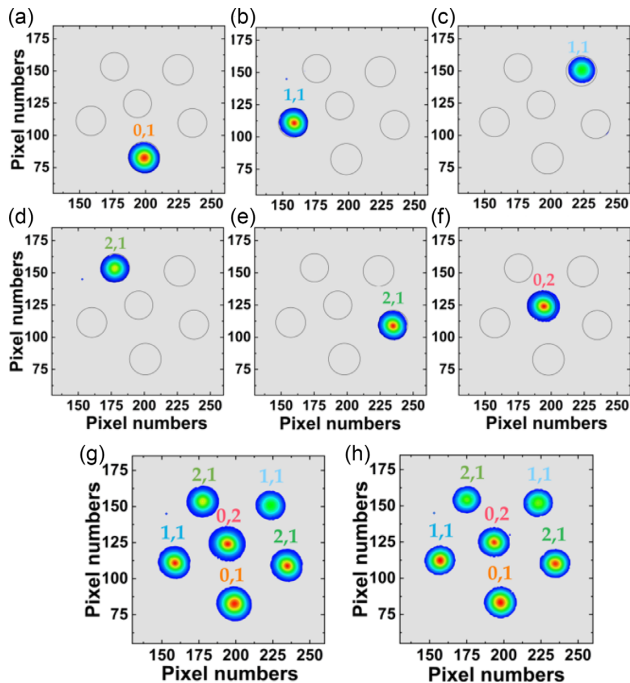


Figure 4. (a)–(f) Near-field images of the output in each MCF core using light at around 1550 nm. (g) & (h) Composite images of the outputs. In (g), the excitation is optimized to maximize power transmission. In (h) the excitation is deliberately misaligned in an attempt to excite any higher order modes supported by each core.

results confirm the first cross-talk measurement between the two smallest cores (which are most likely to couple) of <0.08 per cent in 2 m (Yerolatsitis 2017), which is sufficiently low to ensure no observable excitation of unwanted light due to coupling between adjacent cores. Fig. 4(g) is a composite of Figs 4(a)–(f) and (h) is a similar composite but with the fibres slightly misaligned by a lateral offset of the input SMF fibre relative to the MCF using a three-axis translation stage. The light patterns were unaffected by the input excitation even for the largest core, despite its larger mismatch with the SMF (core diameter 7 versus 11 μm and NA 0.22 versus 0.11, respectively). This invariant light pattern demonstrates demonstrating the single-mode nature of each core at 1550 nm.

3 THE PHOTONIC LANTERN TRANSITIONS

The optimum MCF core arrangement was investigated by simulating, using the finite-element method, the evolution of the effective index of the guided modes as a function of the taper ratio (ρ) for the first seven modes of the MCF, where the seventh mode is the lowest order cladding mode. This was repeated for all 720 possible permutations of cores over the same set of six locations, the aim being to equalize the effective index separation of the modes along the transition and thus minimize mode coupling; the optimum is shown in Fig. 5. An MCF was then fabricated with this design (Yerolatsitis 2017). A PL was fabricated at one end of 7 m of MCF using established tapering techniques (Yerolatsitis 2014). The profile of the taper was approximately linear with a length of 3 cm for a taper ratio of 0.09. The cleaved end of the taper had a multimode core with a diameter of 12 μm and an NA of 0.22 (Yerolatsitis 2017). To investigate the mode-selective properties of the PL transition we used the system described in Section 2. Light at 1550 ± 20 nm was coupled into each MCF core individually, and the output of the PL was imaged (Fig. 6).

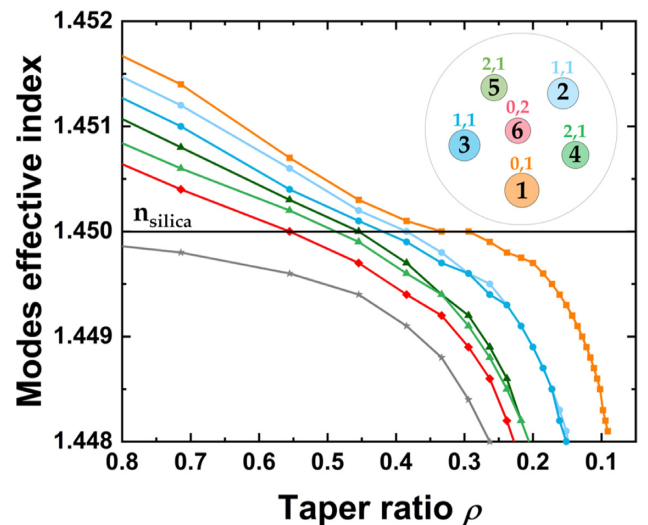


Figure 5. Evolution of the mode effective index as a function of the taper ratio ρ for the first seven modes of the multicore fibre calculated by the finite-element method. Inset: schematic representation of the cross-section of the MCF with the associated colour pattern of each mode. The cores are numbered 1–6 in decreasing order of size, and increasing order of the mode excited in the PL. The pairs of numbers indicate the LP mode designation – for example, core 2 excites an $\text{LP}_{1,1}$ mode.

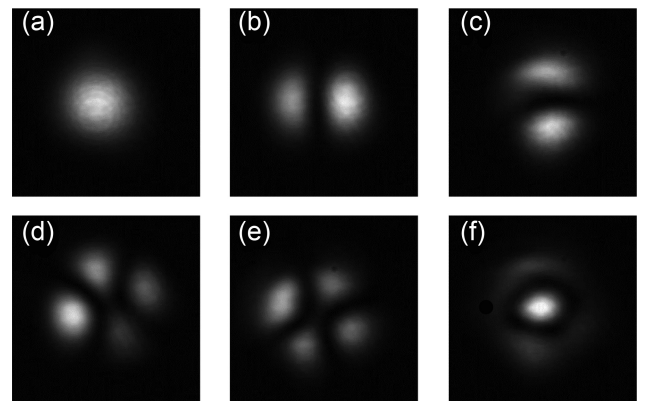


Figure 6. Near-field images of the PL output while coupling 1550 nm light into the opposite end of the 7 m long MCF. Figs (a), (b), (c), (d), (e), and (f) were obtained while individually exciting the MCF cores labelled 1, 2, 3, 4, 5, and 6, respectively in Fig. 5. The patterns closely resemble the $\text{LP}_{0,1}$, $\text{LP}_{1,1}$, $\text{LP}_{1,1}$, $\text{LP}_{2,1}$, $\text{LP}_{2,1}$, and $\text{LP}_{0,2}$ modes, respectively.

Each MCF core excites a specific LP mode at the MMF port of the PL – clear evidence of the mode-selective nature of the PL and the minimally coupled cores at 1550 nm. To confirm the suitability of the PL transition for an FRD mitigation application, we investigated its mode coupling properties using the experiment shown in Fig. 7(a). A thermal tungsten light source (Thorlabs SLS201L/M) was used to generate broad-band light from the visible to the near-infrared. This light was coupled into a 400 μm diameter fibre which was used to transmit the light to the characterization system. The light emerging from this fibre was collimated with a diameter of 8 mm by lens L1, and coupled through a bandpass filter to select the wavelength band for the measurement. An adjustable graduated pinhole was used to restrict the diameter of the collimated beam, and thus the f-ratio of the light focused by lens L2 on to the MMF port of the PL. At high f-ratio excitation, only the fundamental mode (orange squares)

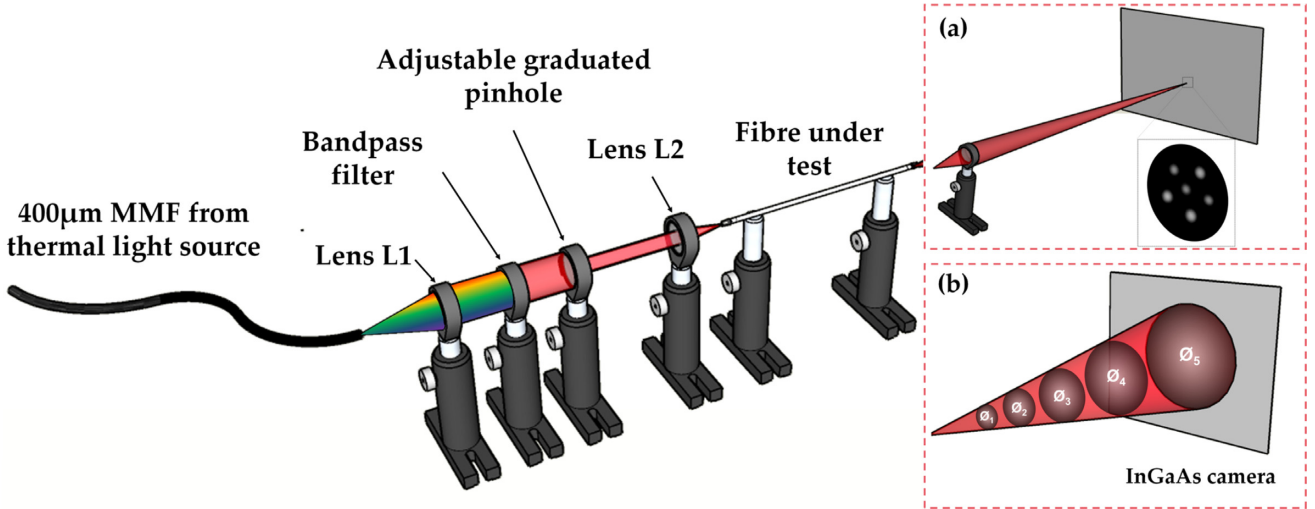


Figure 7. Schematic of the experiment used to characterize the guiding and FRD properties of our fibre devices. Light from the thermal light source was coupled into a 400 μm core fibre. This light was collimated by lens L1 and passed through a bandpass filter to control the wavelength of the light. The filtered light was then passed through an adjustable graduated pinhole to control its diameter and coupled into lens L2 to excite the fibre under test. The f-ratio was controlled via the adjustable pinhole. At the output of the fibre we could either use system (a) to characterize the near-field intensity distribution, or system (b) to characterize the f-ratio of the output. In both cases, light detection is performed using an InGaAs camera.

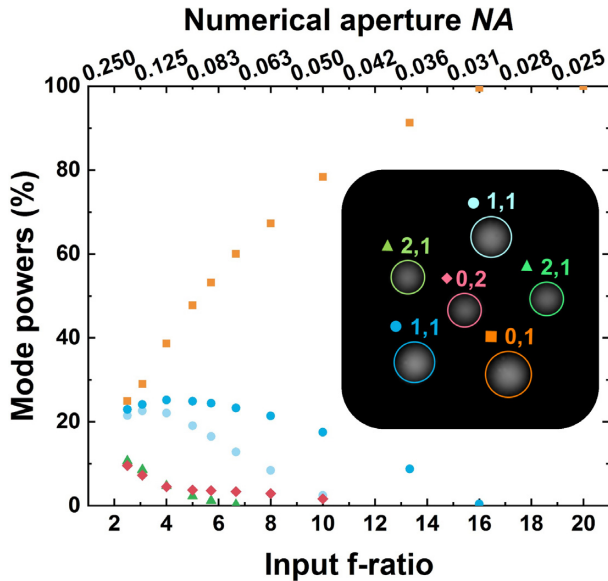


Figure 8. Evolution of the relative power of each mode at the output of the MCF as a function of the f-ratio of the light used to excite the PL. Inset: A near-field image of the MCF output when the PL is excited using low f-ratio light. Each core is labelled to indicate the LP mode to which it is coupled at the input of the PL. The evolution is described in Fig. B1 in the Appendix A and is presented in Visualization 1.

is excited in the multimode port of the PL, and as a consequence light only emerges from the bottom right MCF core. As the input f-ratio reduces, higher order modes are increasingly excited in the multimode port and light becomes increasingly distributed across all the cores of the MCF. In effect, the PL is functioning as a mode analyser. All the different steps of the evolution of the output light core distribution versus input f-ratio are presented in Fig. B1 in Appendix A and are animated in Visualization 1. The output of the MCF was imaged on to an InGaAs camera to view the distribution of the light across its cores. Fig. 8 summarizes the evolution of the

relative power contained in each core as a function of the excitation f-ratio and (inset) the MCF output measured under the lowest f-ratio excitation (Unlike Fig. 4, this is not a composite image).

4 THE FRD MITIGATION MULTIMODE FIBRE LINK

The full FRD mitigation PL-MCF-PL link was realized by fabricating mode-selective PL transitions at both ends of the 7 m MCF. FRD performance was characterized using the system in Fig. 7(b). Fig. 9 (red circles) presents the output f-ratio of the PL-MCF-PL link as a function of the input f-ratio, the latter being the ratio of the focal length of L2 to the diameter of the adjustable graduated pinhole. These results were obtained using 1550 ± 20 nm light, the wavelength for which the MCF cores were designed to be single mode and minimally coupled. To compare its FRD to a conventional multimode fibre, we also fabricated a step-index Ge-doped fibre that supported six modes at 1550 nm (6-MMF). The 6-MMF had a core diameter of 10.4 μm , an 80 μm diameter cladding, and a numerical aperture of 0.22. Both fibre devices were held as straight as possible over the same length of 7 m. Fig. 9 (blue squares) presents FRD data taken for 6-MMF. As described in the Appendix B, each data point is the average of five measurements, and the error bars represent the minimum and maximum measured values. One can clearly observe the difference in FRD mitigation performance between the two fibre links in Fig. 9, with the PL-MCF-PL link exhibiting a significant improvement in FRD performance than 6-MMF. This result demonstrates the potential of our PL-MCF-PL based approach to FRD mitigation in fibre-fed instrumentation (Benoît 2019).

Clearly, we have used different experimental methods to quantify the f-ratio of the light used to excite the fibre link, and the f-ratio of the light exiting the fibre link. As a result, caution is required when directly comparing the absolute magnitudes of these two f-ratio measurements. Regardless, since our f-ratio measurement methods do not change for different fibre links, our experimental approaches

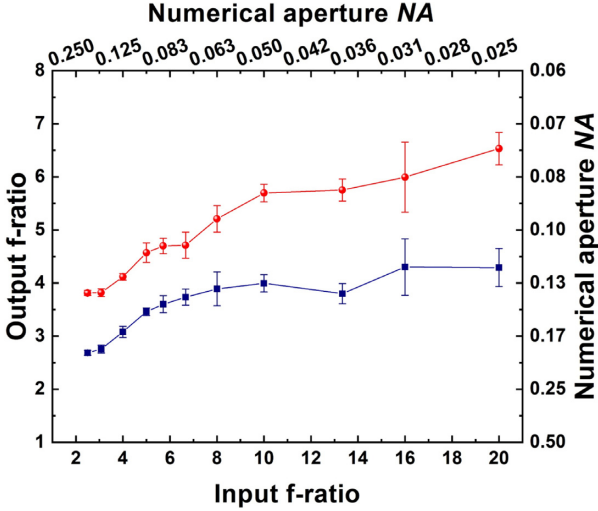


Figure 9. Output f-ratio versus input f-ratio measured for the 6-MMF (blue squares) and the PL-MCF-PL link (red points), at the wavelength of 1550 ± 20 nm.

are adequate and appropriate to observe qualitative differences in the FRD performance of different multimode fibre links.

Finally, Fig. 9 shows another interesting aspect in the global evolution of the output f-ratio for the two fibres. The 6-MMF fibre follows the expected behaviour as shown in Fig. 1. However, the PL-MCF-PL presents a general slope closer to the ideal 1:1 with increasing input f-ratio until 10, and when the fundamental mode begins to be the only mode that can be excited, the global slope is closer to the upper limit described in our schematic example in Fig. 1. This f-ratio degradation might be due to unwanted mode mixing in the transition which can cause a lower output f-ratio. In addition, the PL-MCF-PL supports only a few modes and therefore we would expect a staircase line rather than a straight 1:1 line, where each step corresponds to a different mode group. To investigate how the FRD mitigation varies with wavelength, we repeated the measurements for wavelengths of $1424 \text{ nm} \pm 42 \text{ nm}$ and $1064 \text{ nm} \pm 25 \text{ nm}$, selected by changing the bandpass filter. Fig. 10(a) shows the evolution of the output f-ratio as a function of the input f-ratio for the PL-MCF-PL link, with the red circles, green diamonds, and blue triangles representing data at 1550, 1424, and 1064 nm, respectively. Again, each data point is the average of five measurements, and the error bars represent the minimum and maximum values. A full description of the data acquisition and data processing for all the output f-ratio measurements is presented in Appendix B. A number of interesting features can be observed in Fig. 10(a). It is clear, for example, that the minimum output f-ratio decreases with decreasing wavelength, and that the overall FRD performance of the PL-MCF-PL link degrades with decreasing wavelength. This, we believe, is primarily because the PL transitions of the PL-MCF-PL link become progressively less adiabatic as the wavelength is reduced. As a result, higher order modes are excited at both the input and output PLs, decreasing the output f-ratio and degrading the FRD properties. Figs 10(b)–(c) and Figs 10(d)–(e) represent similar characterization results to those presenting in Figs 4(g)–(h) using 1550 nm light, but this time using light at 1424 and 1064 nm and either optimized (b & d) or non-optimized input excitation positions (c & e). One can clearly observe that the larger cores become progressively multimode when the wavelength is reduced. These higher order modes can more efficiently cross-couple within the MCF than the smaller fundamental

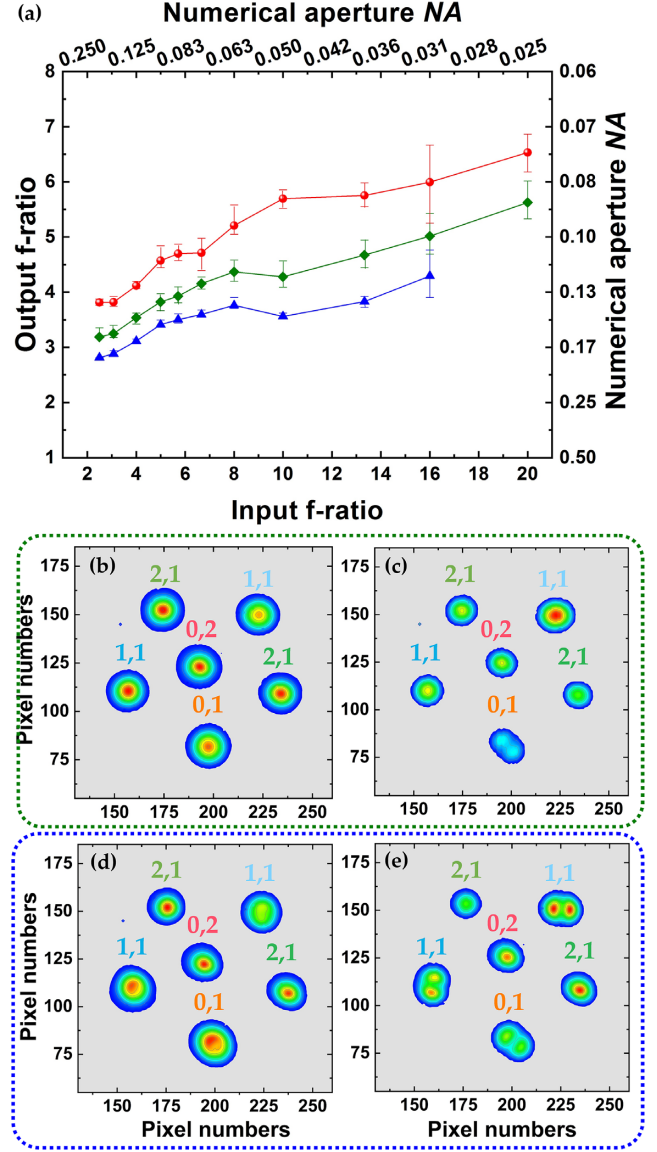


Figure 10. (a) Output f-ratio versus input f-ratio measured for the PL-MCF-PL at the wavelengths of $1550 \text{ nm} \pm 20 \text{ nm}$ (red circles), $1424 \text{ nm} \pm 42 \text{ nm}$ (green diamonds), and $1064 \text{ nm} \pm 25 \text{ nm}$ (blue triangles). (b)–(e) Composite near-field images of the MCF output (no PL transitions) when exciting individual MCF cores using either (b & c) $1424 \text{ nm} \pm 42 \text{ nm}$ or (d & e) $1064 \text{ nm} \pm 25 \text{ nm}$ light. In (b & d) the input excitation is optimized, and in (c & e) the input excitation is non-optimized to excite higher order modes.

modes, further degrading the FRD performance of the fibre link. The higher order modes supported by the cores facilitate cross-talk along the MCF, and induce FRD through the transfer of energy from lower order modes at the input to higher order modes at the output.

5 CONCLUSIONS

We have reported FRD mitigation in a multimode fibre link using an MCF with mode-selective PLs. The MCF has six Ge-doped step-index cores with dissimilar diameters, and sufficient intercore separations to minimize intercore cross-talk over the length of fibre used. The FRD mitigation was achieved by fabricating mode-selective PLs at each end of the MCF. When tested at 1550 nm, the FRD behaviour of the PL-MCF-PL link is superior to that of a step-

index MMF that also supports six modes. We believe this is due to the manner in which the PL-MCF-PL link inhibits the transfer of energy from low-order modes at the input PL to high-order modes at the output PL. FRD was observed to become increasingly pronounced as the excitation wavelength was reduced from the design wavelength of 1550 nm – a behaviour that we attribute to the fact that the PLs either end of the PL-MCF-PL link become progressively less adiabatic as the wavelength is reduced, and due to the increasingly multimode nature of the MCF cores, which then facilitates core-to-core cross-talk.

In summary, we have demonstrated how MCFs and mode-selective PLs open an entirely new route to control and mitigate FRD in multimode fibre links, with considerable potential to impact the design of fibre-fed instruments in fields such as astronomy. Our approach is applicable to other regions of spectrum, such as the visible, by fabricating a scaled version of the MCF. We believe that the concept we have presented here could be extended to fibre links operating with many 10's of modes. This would involve developing MCF's with more cores in proportion to the number of modes required and optimizing the position of each core in the multicore fibre to aid the mode-selectivity of the PL transitions. If this MCF had the same length and was made of the same core and cladding materials as the MCF used in this work, both the core-to-core separation and the range of core sizes would need to be maintained, in order to keep the cores optically isolated from one another and maintain their single-mode and well-guided optical properties. This would increase the fibre's diameter. If, however, the MCF was fabricated using more-exotic silicate glass materials which are still suitable for fibre tapering but allow a much larger range of refractive indices (Morova 2019), or even use air as a second cladding to inhibit core-to-core coupling in the MCF (Wood 2018), it should be possible to develop more-compact MCFs supporting many 10's of optically isolated single modes suitable for the FRD-mitigation application.

Clearly, the cross-coupling of light within the MCF is just one of the challenges that need to be overcome, and we note that the mode-selectivity of the PL transition becomes harder as the number of cores increases (Yerolatsitis 2014). We also note, however, that this can be mitigated by only requiring PL transitions that are mode-group-selective, rather than selective for individual modes. Instead of maintaining the distribution of light within a group of modes, all of which exhibit similar NAs, such a device would maintain the distribution of light between different mode groups. For example, a suitable MCF could have six different core sizes like the MCF reported here, but several cores of each size. The maintenance of focal-ratio will then be as fine-grained as the number of core sizes, rather than the number of cores.

ACKNOWLEDGEMENTS

This work was funded by the UK STFC through grants ST/N000544/1 and ST/N000625/1, and by the European Union Horizon 2020 grant 730890 (OPTICON).

DATA AVAILABILITY

Raw data will be made available on the Heriot-Watt University PURE system (Available at <https://doi.org/10.17861/affbdaf5-96d2-4f31-9fcd-5910021049e4>).

REFERENCES

- Angel J. R. P., 1977, *AJ*, 218, 776
 Barden S. C., 1994, in Pyper D. M., Angione R. J., eds, ASP Conf. Ser. Vol. 55, Optical Astronomy from the Earth and Moon. Astron. Soc. Pac., San Francisco, p. 130
 Barden S. C., Ramsey L. W., Truax R. J., 1981, *Astron. Soc. Pac.*, 93, 154
 Benoît A., 2019, Conference on Lasers and Electro-Optics Europe and European Quantum Electronics Conference (CLEO/Europe-EQEC), Optical Society of America, OSA, paper CJ14.6
 Birks T. A., 2012, *Opt. Expr.*, 20, 13996
 Birks T. A., 2015, *Adv. Opt. Photon.*, 7, 107
 Bland-Hawthorn J., 2010, in McLean I. S., Ramsay S. K., Takami H., eds, Proc. SPIE Conf. Ser. Vol. 7735, Ground-based and Airborne Instrumentation for Astronomy III. SPIE, Bellingham, p. 77350N
 Bland-Hawthorn J., 2011, *Nat. Commun.*, 2, 581
 Bryant J. J., 2014, *MNRAS*, 438, 869
 Bryant J. J., Bland-Hawthorn J., 2012, in McLean I. S., Ramsay S. K., Takami H., eds, Proc. SPIE Conf. Ser. Vol. 8446, Ground-based and Airborne Instrumentation for Astronomy IV. SPIE, Bellingham, p. 84466K
 Carrasco E., Parry I. R., 1994, *MNRAS*, 271, 1
 Clayton C. A., 1989, *A&A*, 213, 502
 Colless M., 2001, *MNRAS*, 328, 1039
 Finstad D., 2016, *App. Opt.*, 55, 6829
 Gris-Sánchez I., 2018, *MNRAS*, 475, 3065
 Horton A., 2011, CLEO Pacific Rim, Optical Society of America, OSA, paper JSIII P9
 Leon-Saval S. G., 2005, *Opt. Lett.*, 30, 2545
 Li J., 2018, *APL Photon.*, 3, 100902, 1
 MacLachlan D. G., 2017, *MNRAS*, 464, 4950
 Malinauskas M., 2012, *Light: Sci. Appl.*, 5, e16133
 Mayor M., 2003, *Messenger*, 114, 20
 Morova B., 2019, *Opt. Expr.*, 27, 9502
 Murphy J. D., 2008, in Atad-Etchedgui E., Lemke D., eds, Proc. SPIE Conf. Ser. Vol. 7018, Advanced Optical and Mechanical Technologies in Telescopes and Instrumentation. SPIE, Bellingham, p. 70182T
 Noordegraaf D., 2009, *Opt. Expr.*, 17, 1988
 Oliveira A. C., de Oliveira L. S., dos Santos J. B., 2005, *MNRAS*, 356, 1079
 Parry I. R., 2006, *New Astron. Rev.*, 50, 301
 Poppett C. L., Allington-Smith J. R., 2007, *MNRAS*, 379, 143
 Ramsey L. W., 1988, in Barden S. C., eds, ASP Conf. Ser. Vol. 3, Fiber Optics in Astronomy. Astron. Soc. Pac., San Francisco, p. 26
 Richardson D. J., 2013, *Phil. Trans.*, 374, 02140441
 Wood H. A. C., 2018, *Opt. Lett.*, 43, 5311
 Yan Y., 2017, *MNRAS*, 466, 1669
 Yan Y., 2018, *MNRAS*, 46, 4279
 Yerolatsitis S., 2014, *Opt. Expr.*, 22, 608
 Yerolatsitis S., 2017, Optical fibre Communication conference. Optical Society of America, OSA, paper Tu3J.6
 Yin M.-J., 2018, *Coord. Chem. Rev.*, 376, 348

SUPPORTING INFORMATION

Supplementary data are available at *MNRAS* online.

Visualization.mp4

Please note: Oxford University Press is not responsible for the content or functionality of any supporting materials supplied by the authors. Any queries (other than missing material) should be directed to the corresponding author for the article.

APPENDIX A: MCF POWER DISTRIBUTION AFTER THE PL

In the ideal case, a mode-selective PL couples each spatial mode of its multimode port to a specific single mode core at its output. We therefore expect that since different spatial modes of the multimode port are excited as the f-ratio of the excitation light is varied, the distribution of light across the MCF cores will also change. We characterized this and presented the results in Fig. 6 and Fig. B1 presents the full results. The f-ratio of the excitation light is indicated in the bottom left of each subfigure. This full sequence is presented in the Visualization 1. As can be seen in Fig. B1, the light becomes progressively more localized into fewer and fewer MCF cores as the excitation f-ratio is increased. This behaviour is most pronounced when an excitation f-ratio of 20 is used. Under this case, only the fundamental mode of the multimode port of the PL is efficiently excited, which then excites only one core of the MCF at the output.

APPENDIX B: FRD DATA ACQUISITION AND PROCESSING

The aim of the experiment is to measure how the f-ratio of the light emerging from the fibre link under test varies as we adjust the f-ratio of the excitation light.

A variety of different methods have been used to characterize the FRD of multimode fibres. These can involve the use of angled or non-angled input beams, and the detection of either collimated or uncollimated output light (Barden 1981; Ramsey 1988; Carrasco & Parry 1994; Finstad 2016). For our purposes, we chose to use a collimated input beam that is focused on to the input of the fibre link under test with a variable f-ratio. At the output of the fibre link under test, we measure the f-ratio of the emerging light using an InGaAs camera. The experimental setup is described in Fig. 7(b). The full data processing from the five raw image acquisitions to a final output f-ratio value follows these main steps:

B1 STEP 1 – Raw data

Acquisition of the five raw output beam images (\emptyset_1 to \emptyset_5 in Fig. 7(b)) from the fibre link under test with the InGaAs camera placed on a translation stage for each input excitation f-ratio (Fig. B2(STEP 1)). The first position (\emptyset_1) of the camera in front of the fibre link under test is optimised to obtain the best signal to noise. From \emptyset_1 to \emptyset_5 , the camera is translated by 0.2 mm between each measurement. For the input f-ratio beyond 10, this movement was reduced to 0.1 mm due to the diminution of the input power with a smaller adjustable graduated pinhole.

B2 STEP 2 – Virtual knife edge technique

To avoid assuming any specific beam shape, a virtual knife-edge technique is used on the raw images to integrate each column and obtain an S-shaped cumulative curve (Fig. B2(STEP 2)).

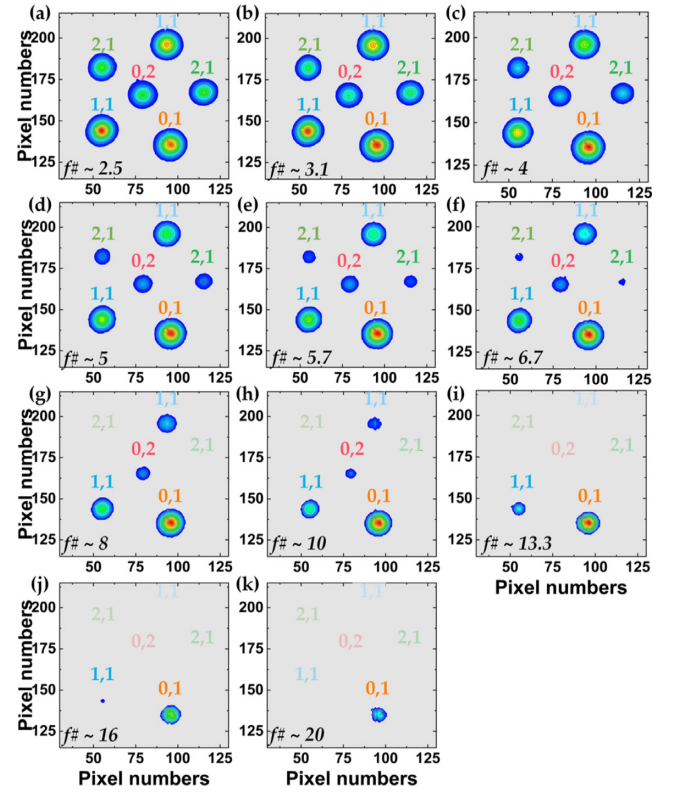


Figure B1. (a)–(k) Evolution of the near-field intensity distributions of the output MCF as a function of the excitation f-ratio from (a) the largest pinhole diameter to (k) the smallest.

B3 STEP 3 – Determination of 95 per cent of the beam

A derivative function is applied to this cumulative S-curve to achieve recover a realistic shape of the emergent beam which is normalized. For the smallest output beam (highest f-ratio), the beam size is just described by a few points. A linear extrapolation allows us to correctly define the encircled energy at 95 per cent of the full beam diameter, as shown by the blue arrow in (Fig. B2(STEP 3)).

B4 STEP 4 – f-ratio value

With the five beam size measurements at 95 per cent of the beam (black squares in (Fig. B2(STEP 4))), a linear fit is applied to smooth the extrapolation and to increase the precision, giving five new beam sizes (\emptyset_1 to \emptyset_5 in green). A f-ratio value is then calculated for each comparison between two beam sizes, \emptyset_1 and \emptyset_2 , \emptyset_1 and \emptyset_3 etc.

B5 STEP 5 – Final f-ratio value

The same process was repeated five times. All the f-ratio measurements in Figs 9 and 10 are an average of five measurement campaigns, with the maximum and minimum values giving the error bars (Fig. B2(STEP 5)).

MEASUREMENT CAMPAIGN

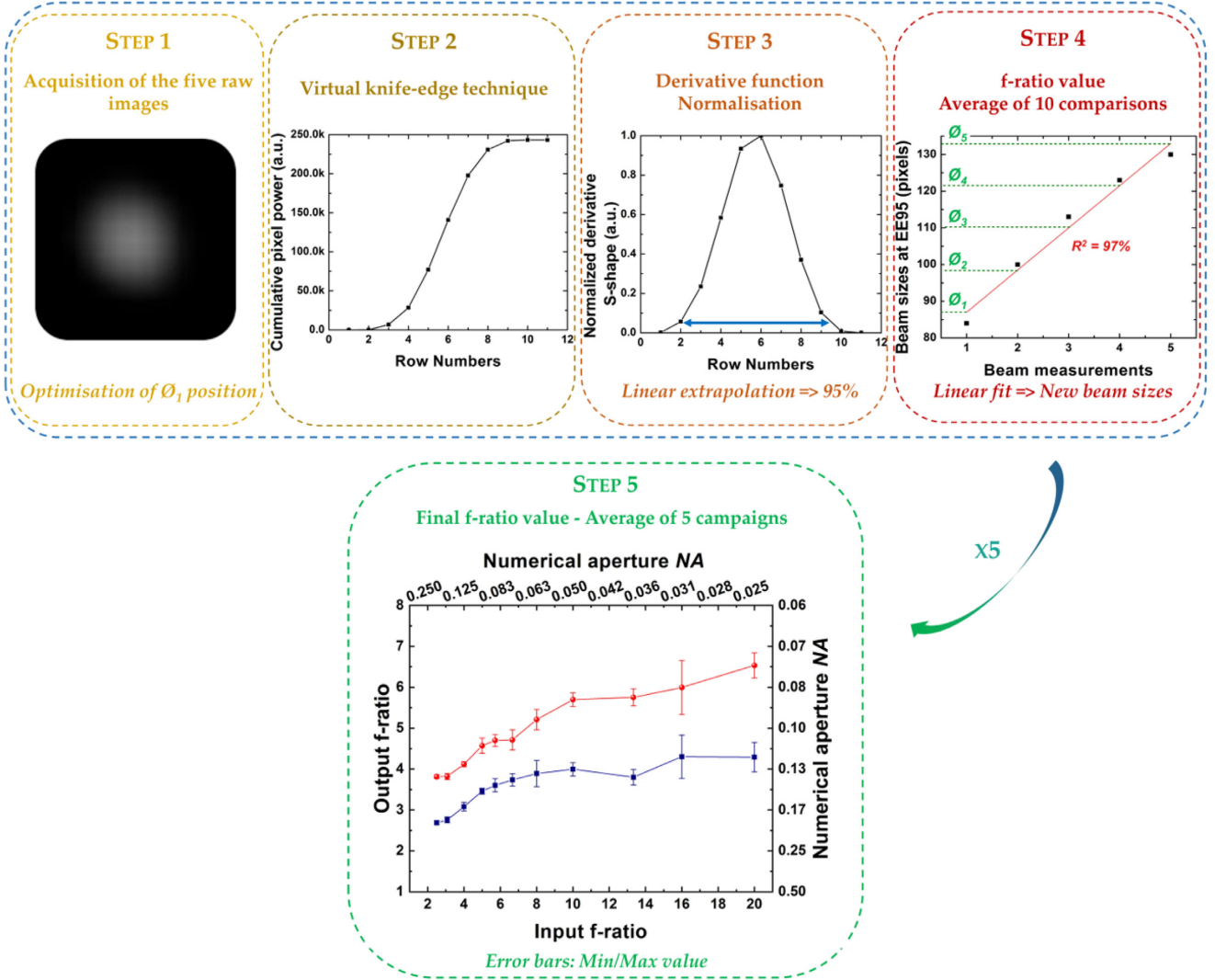


Figure B2. Steps used to process the raw data acquired to measure the output f-ratio. STEP 1: the InGaAs camera is used to capture the output beams at different distances from the output of the fibre link under test. STEP 2: a virtual knife-edge technique is used to integrate the beam shown in STEP 1. STEP 3: the data in STEP 2 is then differentiated and normalized. The blue arrow represents the measurement of the encircled energy at 95 per cent of the beam size. STEP 4: a linear fit (red line) is applied to the five beam sizes from STEP 3 (black squares) to determinate precisely the five new beam sizes (from \emptyset_1 to \emptyset_5 in green) and calculate an output f-ratio value. STEP 5: The measurement campaign is reproduced 5 times to calculate the final f-ratio value. This figure presents an example of the data acquisition and processing for the mode-selective PL at an excited f-ratio of 13.

This paper has been typeset from a \LaTeX file prepared by the author.